

Energy & Environmental Science

Accepted Manuscript

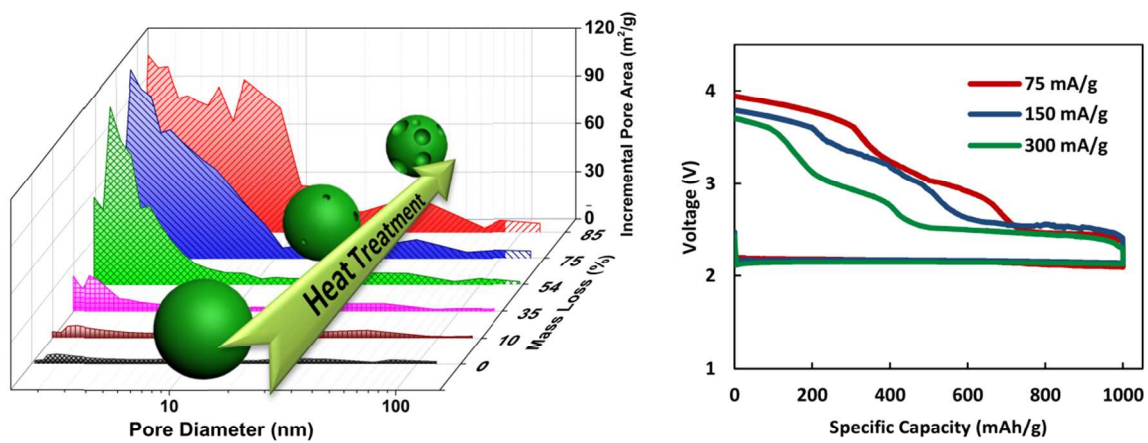


This is an *Accepted Manuscript*, which has been through the Royal Society of Chemistry peer review process and has been accepted for publication.

Accepted Manuscripts are published online shortly after acceptance, before technical editing, formatting and proof reading. Using this free service, authors can make their results available to the community, in citable form, before we publish the edited article. We will replace this *Accepted Manuscript* with the edited and formatted *Advance Article* as soon as it is available.

You can find more information about *Accepted Manuscripts* in the [Information for Authors](#).

Please note that technical editing may introduce minor changes to the text and/or graphics, which may alter content. The journal's standard [Terms & Conditions](#) and the [Ethical guidelines](#) still apply. In no event shall the Royal Society of Chemistry be held responsible for any errors or omissions in this *Accepted Manuscript* or any consequences arising from the use of any information it contains.



Chemical composition of the discharge products as well as charging overpotential of Na-air cell is correlated to the kinetic parameters.

ARTICLE

On Rechargeability and Reaction Kinetics of Sodium-Air Batteries

Cite this: DOI: 10.1039/x0xx00000x

Hossein Yadegari^a, Yongliang Li^a, Mohammad Norouzi Banis^a, Xifei Li^a, Biqiong Wang^a, Qian Sun^a, Ruying Li^a, Tsun-Kong Sham^b, Xiaoyu Cui^c and Xueliang Sun^{a,*}Received
Accepted

DOI: 10.1039/x0xx00000x

www.rsc.org/

Rechargeable metal-air batteries are widely considered as the next generation high energy density electrochemical storage devices. The performance and rechargeability of these metal-air cells is highly dependent on the positive electrode material, where oxygen reduction and evolution reactions take place. Here, for the first time, we provide a detailed account of the kinetics and rechargeability of sodium-air batteries through a series of carefully designed tests on treated commercial carbon material. Surface area and porous structure of the positive electrode material was modified in order to gain detailed information surrounding the reaction kinetics of sodium-air batteries. The results indicate that discharge capacity is linearly correlated with surface area while morphology of the solid discharge product is strongly dependent on specific surface area and pore size. Furthermore, it was found that the chemical composition of discharge products as well as charging overpotential is affected by discharge reaction rate.

1. Introduction

Wide spread use of fossil fuels in the past few decades, has resulted in a substantial increase to greenhouse gas concentrations and has been a prime contributor to the serious issue of global warming. Since fossil fuels are predominantly consumed for transportation purposes, a switch from the conventional internal combustion engines (ICEs) to electric vehicles (EVs) has received enormous consideration.¹ Furthermore, electric engines have higher conversion efficiency than ICEs making them even more attractive.¹ Lithium-ion batteries (LIBs) have been the technology of choice for application in EVs due to their relatively high volumetric and gravimetric energy density as well as longer battery cycle life in comparison with other available battery systems.² However, current LIB-EVs are restricted to low-mileage applications as a result of limited specific energy density, long charge time as well as high cost.¹⁻³

Metal-air cells, which use a different chemistry from intercalating LIBs, have theoretical specific energy densities high enough to compete with gasoline.^{1,4} The high specific energy densities seen for metal-air batteries is related to the use

of high energy alkaline metals as anodes and oxygen, from ambient air, as cathode materials. Using light metal elements, such as lithium, as the anode material to form a lithium-air (Li-air) battery system has attracted a great deal of attention.⁵⁻⁷ However, large charge overpotentials in these batteries limit their cycle life to less than 100 cycles.⁸ A recently considered alternative metal-air battery is the sodium-air (Na-air) battery, in which lithium is replaced by sodium metal.⁹⁻¹³ Na-air battery systems have a lower theoretical specific energy density (1605 or 1108 Wh/kg considering Na₂O₂ or NaO₂ as discharge products, respectively) compared to Li-air battery systems. However, Na-air batteries also demonstrate lower charge overpotential which may result in better cyclic performance.⁹ Only a few studies address the Na-air battery system⁹⁻¹⁸ with only a limited understanding behind the chemistry of the cell. For instance, various sodium oxides have been reported as discharge products of the Na-air battery system. Fu's et al.^{9,10} has investigated Na-air cells with carbonate and ether based electrolytes while different carbon materials were used as the air electrode. Based on selected area electron diffraction (SAED), their results report the production of sodium peroxide

(Na_2O_2) as a discharge product with the use of either carbonate or ether electrolytes. At the same time, different charge/discharge mechanisms with various discharge products are proposed by Kim et al.¹¹ using carbonate and ether based electrolytes. In this study sodium carbonate and hydrated sodium peroxide were produced as discharge products in carbonate and ether based electrolytes, respectively. More recently, sodium superoxide (NaO_2) has also been shown to be the discharge product of the Na-air battery systems with the use of an ether based electrolyte.^{12,13} In addition, same research group investigated the electrochemistry and thermodynamic of the Na-air cell in a series of systematic studies in which sodium superoxide was the major discharge product.^{14,15} McCloskey et al. also studied the chemical and electrochemical differences of the Na- and Li-air cells and found “cleaner” chemistry in the case of Na-air cell with lower amount of parasitic products during the charge cycle of the cell.¹⁷ The lower amount of decomposition products and hence lower charging overpotential in Na-air cell are related to the more stability of NaO_2 compared to Li_2O_2 as the major discharge products of Na- and Li-air cells, respectively.¹⁷ Meanwhile, Ceder’s research group showed using theoretical calculations that Na_2O_2 is the stable phase in bulk form and NaO_2 is only more stable at nanoscale below 10 nm in particle size.¹⁸ Based on the aforementioned studies, it can be concluded that kinetic factors play a significant role in Na-air cells, resulting in formation of different phases of sodium oxides at various studies.

Even though sodium and lithium share many physiochemical properties, the chemistry of the Li-air and Na-air cells is not the same. While sodium forms stable sodium superoxide, lithium superoxide is thermodynamically unstable.⁹ Therefore, it is expected that both of sodium peroxide and superoxide would be formed under different physiochemical environments, however kinetic factors may stabilize a certain phase over the other oxide. In the present study, we show that the morphology and chemical composition of the discharge products in Na-air battery system depends on various factors including current density and air electrode materials. In addition, charge performance of the Na-air system can be controlled by manipulating the discharge products.

2. Results and discussion

The gas diffusion electrode serves as a diffusing medium for positive active material (oxygen) in metal-air batteries, as well as a substrate for the accumulation of discharge products making the final electrochemical performance of the metal-air system strongly dependent on efficiency of the air electrode. The gas diffusion electrode material used in this work was prepared via heat-treatment of carbon black under various corrosive atmospheres, as outlined in Fig. 1a. Using the heat-treated carbon materials enables the precise control over the porosity and surface area of the air electrode materials. This heated-treated carbon material based on commercially-used carbon black with the post-treatments has been intensively used

in various systems such as fuel cells and high energy batteries.¹⁹⁻²¹ The heat-treated carbon materials allow us to understand correlations between discharge capacity, surface area and porosity of the cathode materials. Carbon black is primarily composed of graphitic crystallites bound together by disordered carbon.²² Heat-treatment of carbon black removes disorder carbon, resulting in a highly porous structure. Micropore boundaries grow with increasing treatment time and eventually result in the formation of mesopores.²² Initially, as treatment time increases, the number of mesopores with a size of less than 10 nm increases while further treatment results in an increases of pore volume. As a result, heat-treated carbons with higher mass losses demonstrate elevated specific surface area values, higher edge to surface ratios, and larger pore size.¹⁹ Nitrogen adsorption/desorption measurements were carried out to illustrate the surface porosity characteristics. The nitrogen adsorption isotherms of the pristine carbon (N330) and heat-treated carbon material under different atmospheres and with various mass losses are shown in supplementary Fig. S1. The pristine N330 carbon presents isotherm of type II, while for heat-treated carbons the type of isotherm is gradually changing from type II to type IV with increase of mass loss. In addition, the nitrogen adsorption ability of heat-treated carbon is also considerably increasing with the increase of mass loss, indicating the increase of the active surface area. The pore size distributions and pore volumes of the carbon materials were obtained from the Barret, Joyner, and Halenda (BJH) analysis using the adsorption branch of each isotherm.

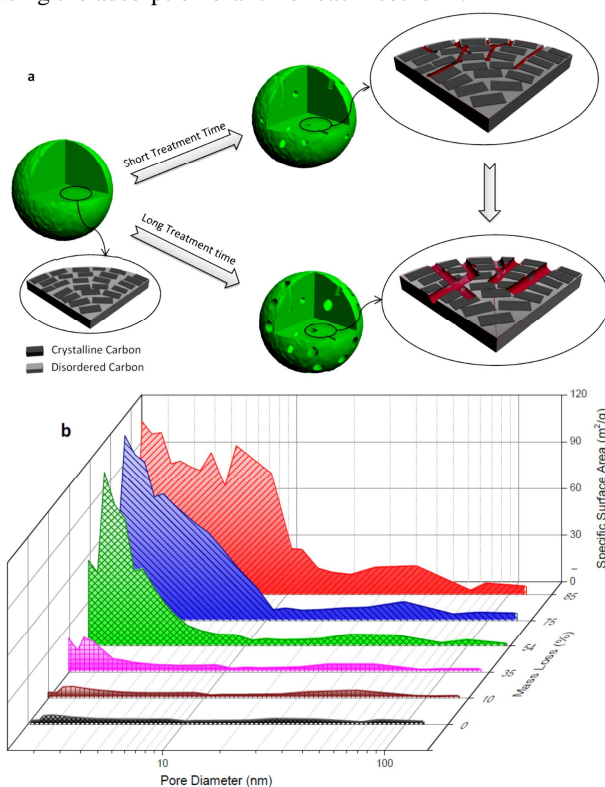


Figure 1: Schematic diagram of carbon black electrode material during the heat-treatment process (a); Pore size distribution plot for NH_3 -treated carbon materials with different mass losses from 0 to 85% (b).

Pore size distribution of NH_3 -treated carbon material is plotted against mass loss, and presented in Fig. 1b (similar data for CO_2 and CO_2/H_2 -treated carbons is shown in supplementary Fig. S2). Heat-treatment of carbon materials under NH_3 , CO_2 , and CO_2/H_2 atmospheres results in a considerable increase to specific surface area in the range of mesopores less than 10 nm (see also supplementary Table S1). The advantage of using heat-treated carbon materials is that various morphologies, surface areas and functional groups can be produced by simply altering pretreatment parameters.

As-prepared carbon materials were tested as gas diffusion electrodes for Na-air cells. Figure 2a shows the discharge curves of different NH_3 -treated carbon samples. All treated carbon materials indicate a flat discharge plateau at 2.2 V, delivering increasing specific discharge capacity with an increase in mass loss (see also Fig. 2b). The plot of specific surface area of treated carbon material as a function of mass loss percentage indicates that specific discharge capacity increases with specific surface area, as shown in Fig. 2b. Specific discharge capacity values increase quantitatively from 505 to 2783 mAh g^{-1} with a mass loss increase of 10 to 85%. In fact, higher surface area presents a greater density of accumulation sites for deposition of solid discharge products, resulting in an increase to the specific discharge capacity of the cell. In addition, a highly porous air electrode structure results in a greater diffusion path for both of oxygen and sodium species, causing decreased mass transfer resistance, and increased cell capacity by postponing the potential drop. Similar trends were also observed for CO_2 and CO_2/H_2 treated carbon materials (supplementary Fig. S3). The specific discharge capacity per actual surface area (calculated based on the specific discharge capacity (mAh g^{-1}) and the specific surface area of the corresponding electrode ($\text{m}^2 \text{g}^{-1}$)) of the electrode materials was plotted as a function of mass loss percentage, as shown in Fig. 2c. Apart from the original N330 sample, all other treated carbon materials demonstrated a constant specific capacity per surface area. These constant values for different treated carbon materials illustrate the substantial effect of surface area on specific capacity for the Na-air battery system. In other words, actual surface area resulting from mesopores of the electrode materials dominantly determines the specific capacity of the air electrode. It should also be noted that the nature of porosity for pristine carbon black is different than other treated carbon materials;^{19,20} the porosity of pristine carbon black originates from pores that exist between carbon particles, and have an average size of 30 nm. The porosity of treated carbon materials, however, stems from mesopores produced during the heat-treatment process and is chemically different in nature. Furthermore, heat-treating of carbon also results in creating small pores in the micropores region. Although these micropores increase the BET surface area, they are not accessible by the electrolyte and hence oxygen diffusion into these micropores is restricted. Therefore, pristine carbon demonstrates higher area-normalized specific capacity compared with heat-treated carbon materials. The total pore volume of heat-treated carbons are also plotted as a

function of mass loss and shown in supplementary Fig. S4. Although the total pore volume of heat-treated carbons also shows a growing trend, but it does not show a direct correlation with specific capacity in Na-air cell.

Morphology of discharge products is another crucial factor that influences the discharge properties of metal-air systems, as well as the charge characteristic and performance of the cell.²³⁻²⁶ Figures 3a-f display SEM micrographs of discharge products for carbon material under various durations of NH_3 treatment. The discharge products observed for pristine carbon black displays rod-shaped particles which are stacked upon each other (Fig. 3a). The rod-shaped particles can also be observed in the case of NH_3 -treated carbons with mass loss of 10-54%. However, as mass loss increases, dimension of discharge products shrink and gradually transform from rod-shaped particles to a thin film structure with a thickness of a few nanometers. The discharge products of treated carbon samples with an elevated mass loss (Fig. 3e and f), predominantly exists as ultrathin nanosheets, uniformly covering the carbon surface. The same morphological changes were also observed for samples treated with CO_2 and CO_2/H_2 (supplementary Fig. S5 and S6). SEM images of initial and charged NH_3 -treated carbon electrode are also shown in supplementary Fig. S7 for comparison purposes.

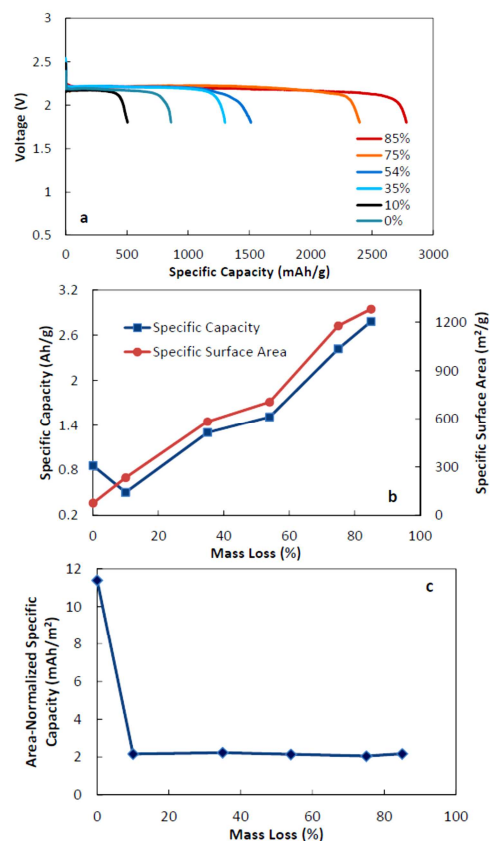


Figure 2: Discharge curves of Na-air cells using NH_3 -treated carbon materials with different mass losses from 0 to 85% as cathode electrode recorded at a current density of 75 mA g^{-1} (a); Plot of specific capacitance and specific surface area of the cathode electrode materials of the cells depicted at Fig. 2a as a function of mass loss (b); Area-normalized specific capacity of the cells depicted at Fig. 2a as a function of mass loss (c).

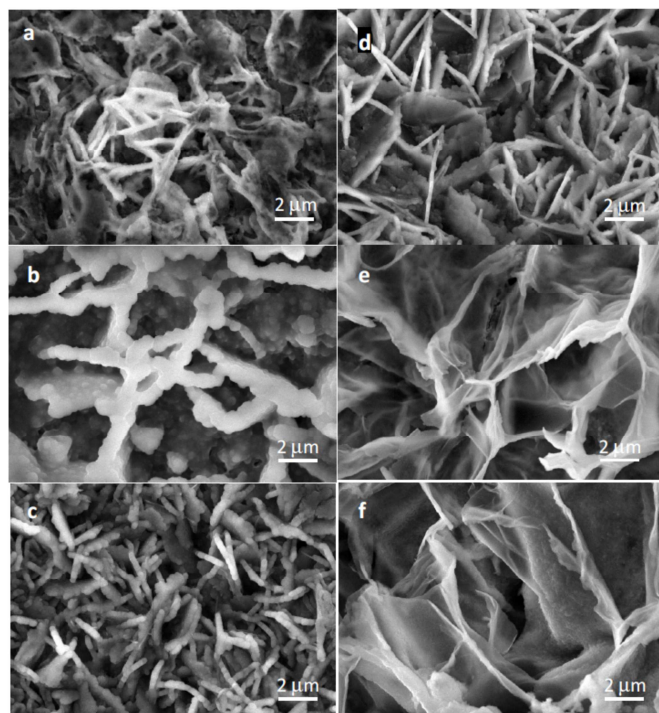


Figure 3: Morphology of discharge products of the Na-air cells using different NH_3 -treated carbon materials with 0 (a), 13 (b), 35 (c), 50 (d), 75 (e) and 85% (f) mass losses as cathode electrode (Discharge current density: 75 mA g^{-1}).

To identify the growth mechanism for the produced nanosheets, morphological changes were observed at different depths of discharge for treated carbon samples with 85% mass loss. The morphologies of discharge products after 8, 16, 24 and 36 hours of discharge are depicted in Fig. 4. Tiny separated fibrils of solid discharge product can be observed after 8 hours of discharge (Fig. 4a), while a major part of the carbon surface is left uncovered. After 16 hours of discharge the initial fibrils increase in size and begin to partially connect with one another in the form of island-shaped structures (Fig. 4b). The same morphology can be observed after 24 hours of discharge, but to a greater extent with a greater degree of connection between the formed islands. Following 36 hours of discharge, the carbon surface is totally covered with a uniform wrinkled film of discharge product (Fig. 4d). The thin layer is composed of interconnected primary discharge particles. More SEM micrographs with various magnifications of positive electrode after multiple steps of discharge process are also shown in supplementary Fig. S8.

The morphology of discharge products can be specified by the equilibrium between nucleation and growth rate. Greater density of nucleation sites, as seen with higher surface area materials, will result in smaller-sized particles being produced. However, lower surface area materials have limited nucleation sites, resulting in the formation of larger-sized particles. Recently, an in-situ AFM study by Wen et al.²⁶ on Li-O_2 electrochemical reaction mechanism revealed that the nucleation process of discharge product (Li_2O_2) mainly occurs

at step edges of the carbon substrate due to the higher surface energy at these locations. The same mechanism is likely to be responsible for different morphologies of discharge products in the Na-air cells. Heat-treatment of carbon materials under corrosive conditions results in the production of new pores, inevitably leading to an increase in edge/plate ratio. The edge plane carbon sites serve as nucleation points for discharge products due to elevated electron transfer reactions occurring at these locations compared to the basal carbon plane.²⁷ As a result, the nucleation rate outpaces the growth rate on the carbon materials with longer treatment time as a consequence of greater edge sites, leading to the dominant production of a film-like structure. The proposed mechanism for discharge product formation is schematically illustrated in Fig. 5. The control of discharge product morphology is critical in rechargeable metal-oxygen battery systems. It is paramount for the produced discharge product to revert back into the starting materials in order for the cell to be considered rechargeable. Solid discharge products larger in size have greater charging overpotential due to their limited interaction with the substrate. In addition, charging overpotential has a smaller value at substrate/discharge product interface (which is accessible by the electrolyte) compared to the bulk of products. Therefore, decomposition process begins at these interfaces. Progression of the decomposition process at interface sites hereupon cuts off the electrical contact to the remaining discharge particles and prevent them to entirely revert back, leading to a limited cycling performance, as reported by Hartmann et al.¹³ However, a uniform thin layer of discharge product may result in enhanced charging process by increasing the interaction between substrate and discharge product.

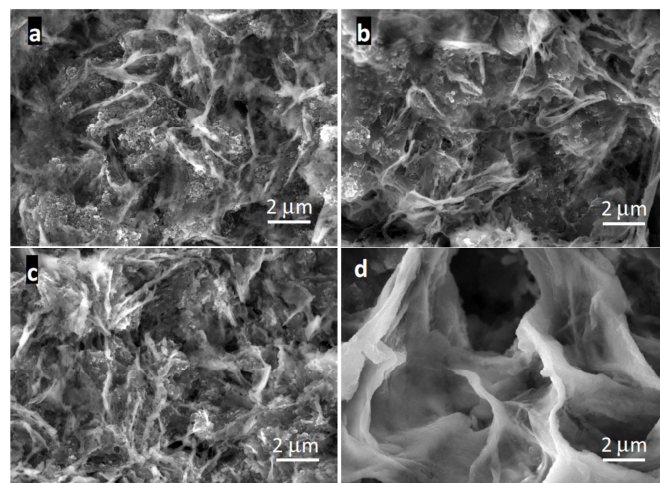


Figure 4: Morphology of discharge products of the Na-air cell using NH_3 -treated carbon material with 85% mass loss as cathode electrode after 8 (a), 16 (b), 24 (c) and 36 (d) hours of discharge (Discharge current density: 75 mA g^{-1}).

To investigate the charging performance of the electrode materials, NH_3 -treated carbon materials with 85% mass loss was subjected to discharge down to a specific capacity of 1.0 Ah g^{-1} and then subsequently charged back at a current density of 75 and 40 mA g^{-1} , respectively as outlined in Fig. 6a. Three

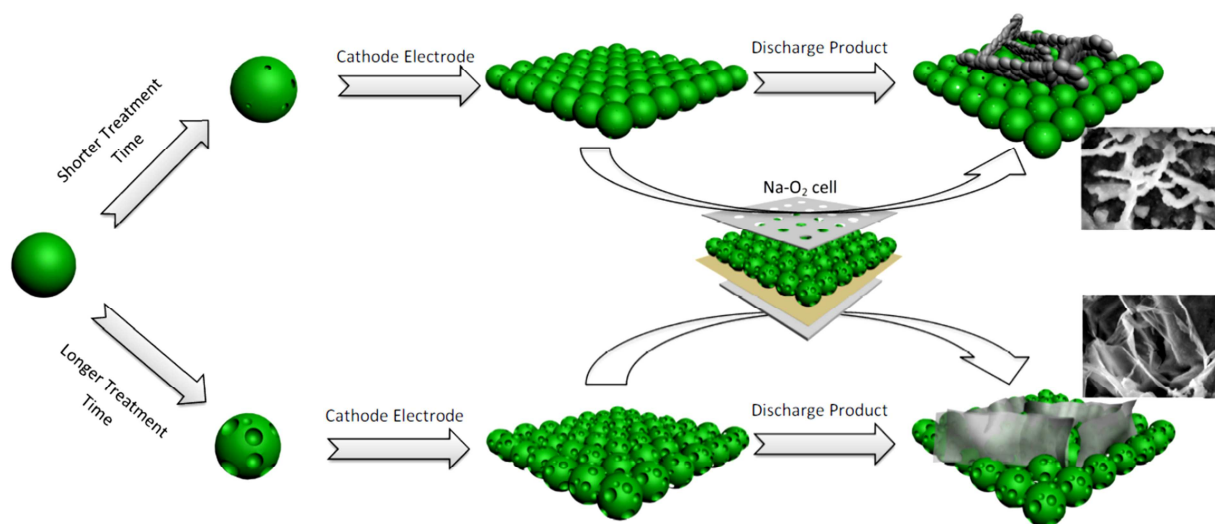
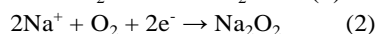
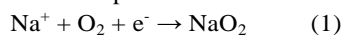


Figure 5: Schematic diagram of Na-air cell using different heat-treated carbon materials as cathode electrode.

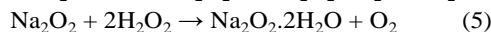
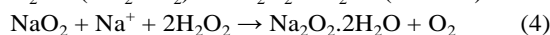
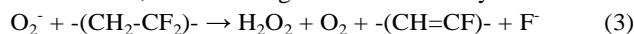
distinct charge regions with a potential range of 2.3-2.75 (region I), 2.75-3.4 (region II) and 3.4-3.9 V (region III) can be distinguished during the charge process. These three charge potential regions will be referred as lower, middle and higher potentials, respectively. Similar charge profiles were observed for CO₂ and CO₂/H₂ treated carbon materials as well (supplementary Fig. S9). Based on the thermodynamic standard potentials of different sodium oxides ($E_{\text{Na}_2\text{O}}^0 = 1.95$, $E_{\text{Na}_2\text{O}_2}^0 = 2.33$ and $E_{\text{NaO}_2}^0 = 2.27$ V)¹² and considering the discharge voltage of the cell (Fig. 2a), the most probable discharge product for Na-air system is either sodium peroxide (Na₂O₂) and/or sodium superoxide (NaO₂). Both of these oxides have been previously reported as major products for Na-air battery systems.⁹⁻¹⁷ However during charging three notable steps are observed, as shown in Fig. 6a, indicating that the charge reaction is not a simple one-species decomposition reaction but rather the formation of multiple initially products produced during discharge.

To better understand the chemistry of Na-air batteries, discharge product of the Na-air cell was examined by X-ray diffraction (XRD) technique. The recorded patterns were obtained from air electrode materials before and after discharge to 1.8 V and are depicted in Fig. 6b. The XRD confirms the existence of multiple discharge products. However, the major discharge product correlates well with hydrated sodium peroxide (Na₂O₂·2H₂O, JCPDS reference card No. 015-0064), as opposed to the expected sodium peroxide. The minor peaks found in the spectrum can be associated with sodium superoxide (NaO₂, JCPDS reference card No. 006-0500). The presence of hydrated sodium peroxide as a discharge product of the Na-air cells using ether (TEGDME) based electrolyte has been previously reported by Kim et al.¹¹ and more recently by Jian et al.¹⁶ Kim et al. have also proposed a reaction mechanism in which TEGDME was subjected to reaction with superoxide ions to produce carbon dioxide and water. However, Nazar et al.²⁵ previously reported in a systematic study on Li-air cell chemistry, that TEGDME does not significantly undergo

decomposition in presence of superoxide ions. However, PVDF readily reacts with this ion and produces hydrogen peroxide.²⁵ In the case of Na-air battery system sodium superoxide can react with hydrogen peroxide to produce hydrated sodium peroxide. Thus, the following mechanism can be adopted for the positive electrode in Na-air cells discharge reactions of Na-air cell at positive electrode can be proposed as follow:



Furthermore, the following side reactions may also occur:



In addition, XRD patterns of positive electrode after charging the cell to 2.75, 3.60 and 4.0 V (corresponding to the various charging steps indicated in Fig. 6a) are shown in supplementary Fig. S10. The peaks related to NaO₂ phase are disappeared after charging the cell to 2.75 V, indicating that the decomposition of NaO₂ takes place at the region I of charge cycle. Charging the cell to 3.6 and 4.0 V results in degradation of peaks related to the Na₂O₂ phase.

Further, discharge products of the Na-air cell after discharge and charge to different potentials (shown in Fig 6a) were also examined by Raman spectroscopy. The resultant spectra combined with reference NaSO₃CF₃, Na₂O₂ and Na₂CO₃ for comparison purposes are depicted in Fig. 6c. The obtained spectra from positive carbon electrode shows two characteristic D and G bands related to the disordered and graphitic carbons, respectively. Additional peak at 1141 cm⁻¹ appeared after discharge of the cell to 1.8 V is related to NaO₂ phase²⁸ which is disappeared after charging the cell to 2.75 V. No Raman peak associating with Na₂O₂ phase was detected, probably due to its weaker Raman signal. Raman and IR spectroscopies are complementary analytical techniques, since transitions allowed in Raman may be forbidden in IR or vice-versa. As a result, the compound with weak Raman signal may show strong absorbance in IR. Accordingly, FTIR spectra of

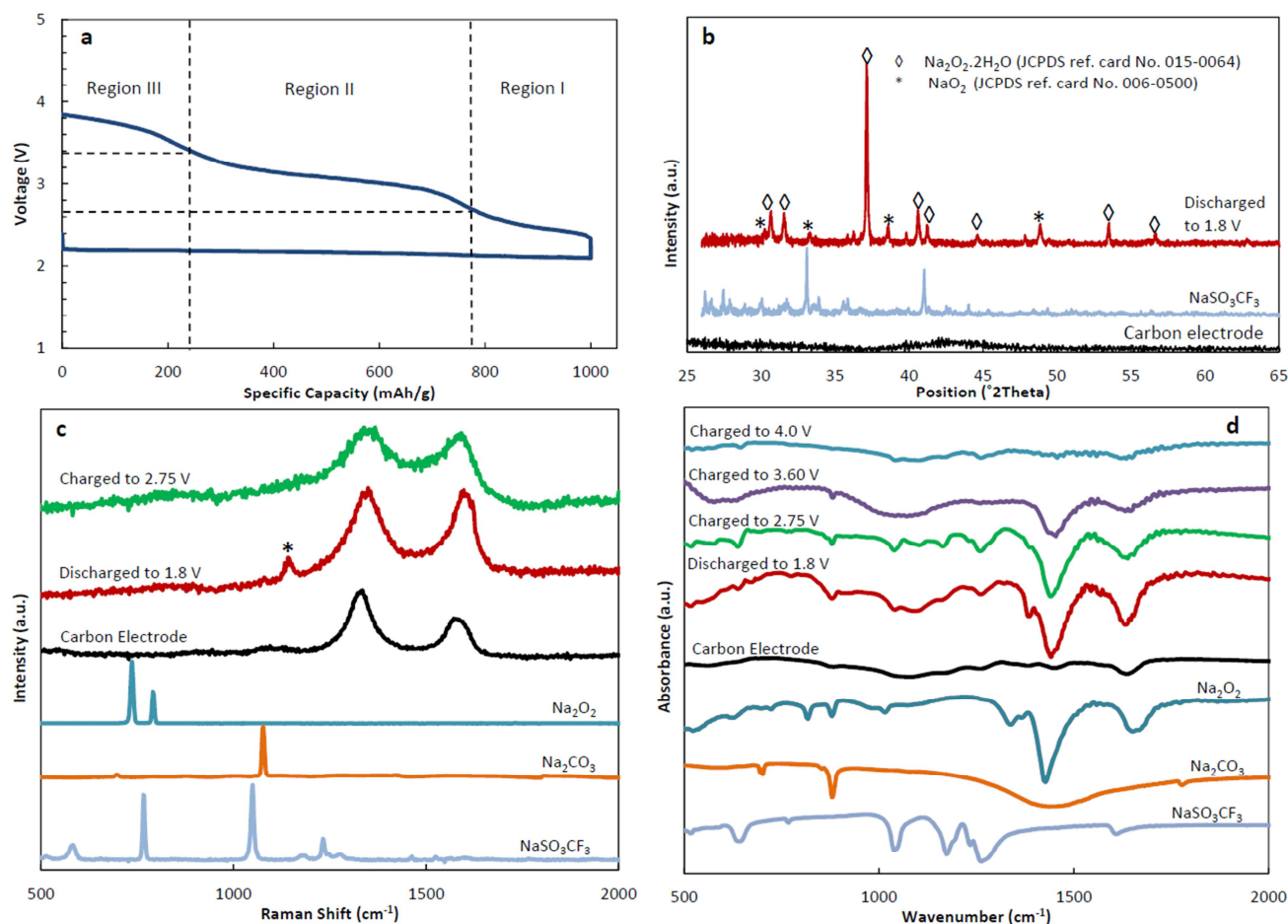


Figure 6: Limited discharge and charge curves of Na-air cell using NH_3 -treated carbon material with 85% mass loss at current densities of 75 and 40 mA g^{-1} , respectively (a); XRD patterns of positive electrode, electrolyte salt and discharge products of Na-air cell shown in panel a (b); Raman spectra of positive electrode after discharge and first charge step shown in panel a, the peak marked with asterisk refers to NaO_2 phase [28] (c); FTIR spectra of positive electrode after discharge and charge to the various regions shown in panel a (d).

positive electrode at different electrochemical states were also recorded, as shown in Fig. 6d. Comparison of FTIR spectra of electrode materials before and after discharge to 1.8 V reveals a characteristic peak at 879 and 1442 cm^{-1} , attributed to Na_2O_2 , providing further evidence as to the production of sodium peroxide during discharge.²⁹ It should also be noted that NaO_2 does not show any characteristic peak in IR due to the homopolar nature of superoxide ion.²⁹ In addition, the Na_2O_2 characteristic peaks remained in the spectra until charging the cell to 4.0 V (corresponding to the region III of Fig. 6a). Based on XRD, Raman and FTIR results, it can be concluded that the charge plateau at lower (region I) and higher (region III) potentials are related to the decomposition reactions of NaO_2 and Na_2O_2 , respectively (see also Fig. 6a). However, deeper understanding about discharge product of the Na-air cell is required to figure out the nature of other charge plateau at middle (region II) potentials.

The formation of superoxide ions is a result of a single electron transfer process resulting in the formation of NaO_2 being kinetically more favorable, while Na_2O_2 is thermodynamically more stable than NaO_2 ($\Delta G_{\text{f}}^0_{\text{Na}_2\text{O}_2} = -449.7 \text{ kJ mol}^{-1}$; $\Delta G_{\text{f}}^0_{\text{NaO}_2} = -218.8 \text{ kJ mol}^{-1}$).^{12,15} Accordingly, the chemical composition

of the discharge product would change under various discharge conditions. To examine this hypothesis, Na-air cells were discharged at different current densities and then charged back under a constant current density. Discharge curves of Na-air cells obtained at different current densities from 75 to 300 mA/g are depicted in Fig. 7a. As discharge current density increases, the discharge voltage and specific discharge capacity decrease slightly. Furthermore, the discharge curve obtained at a current density of 75 mA/g indicates a flat plateau situated at 2.2 V. However, the discharge curve recorded at current density of 150 mA/g shows an initial plateau at around 2.2 V with an additional sloping region at 2.0 V. Similar behavior can also be observed for discharge curve obtained at a current density of 300 mA/g , except for lower discharge voltages mainly because of charge and mass transfer resistances. Based on the standard equilibrium potentials of sodium oxides species, the first (higher potential) and second (lower potential) discharge plateaus can be respectively attributed to the formation of Na_2O_2 and NaO_2 . In addition, a relatively large change can be observed between the discharge capacity for cells discharged at current densities of 75 and 150 mA g^{-1} (compared with the cell discharged at 300 mA g^{-1}), which can be attributed to the

difference between the number of electrons exchanged in equations (1) and (2).

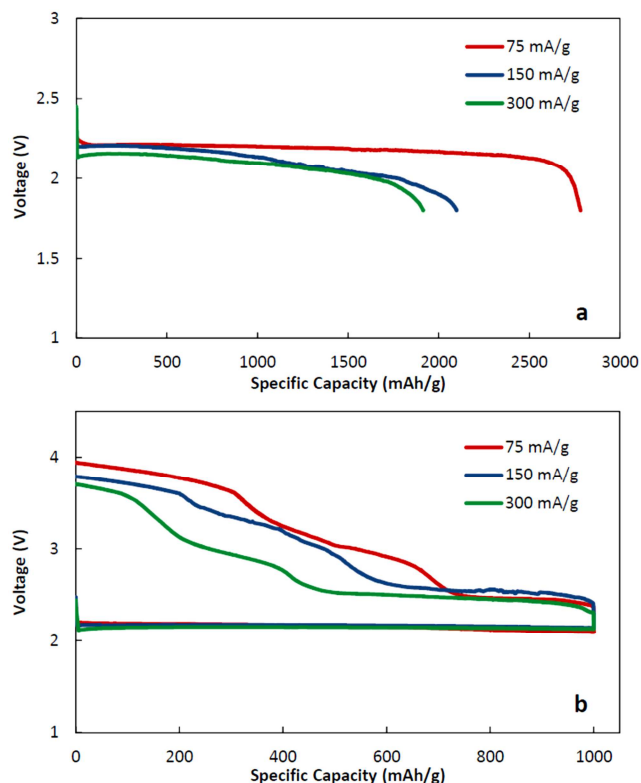


Figure 7: Discharge curves of Na-air cells using NH_3 -treated carbon material with 85% mass loss as cathode electrode recorded at different current densities of 75, 150 and 300 mA g^{-1} (a); Limited discharge and charge curves of Na-air cells using NH_3 -treated carbon material with 85% mass loss as cathode electrode recorded at different discharge current densities of 75, 150 and 300 mA g^{-1} and a constant charge current density of 40 mA g^{-1} (b).

X-ray photoelectron spectroscopy (XPS) analysis was employed to further identify the chemical composition of discharge products at different current densities. Because of the high sensitivity of XPS in analytical speciation measurements, it is chosen to study the chemical composition of discharge products at different current densities. The XPS results for O 1s of reference sodium peroxide and discharge products of the cells discharged at current densities of 75 and 300 mA g^{-1} are depicted in Fig. 8. The spectrum of reference sodium peroxide demonstrates one peak at 530.9 eV related to the peroxide ion and also a small Auger peak around 536 eV (Na KLL).³⁰ The discharged product obtained from lower current densities of 75 mA g^{-1} , shows a similar chemical composition consisting primarily of sodium peroxide. Additional minor fitted peak at 532.3 eV can be correlated to deficient sodium peroxide phase ($\text{Na}_{2-x}\text{O}_2$, vide infra). The discharge product obtained at an elevated current density of 300 mA g^{-1} shows broader XPS peak, indicating wider variety of sodium oxide species. The fitted peaks at 530.9 and 532.3 eV are related to peroxide and deficient sodium peroxide species, respectively. In addition, sodium ion Auger peak is also broader and appeared at higher binding energy which is probably a result of overlapping with superoxide ion peak.³⁰ However, discharge product obtained at

elevated current density of 300 mA g^{-1} exhibit more content of oxygen rich phases which is in accordance with charge and discharge results. The broadening clearly indicates the presence of superoxide (O_2^-), a paramagnetic species which exhibits multiplet splitting (broadening) with one unpaired electron.³¹ Similar conclusion may be obtained from Na 1s spectra shown in supplementary Fig. S11. In addition, XRD patterns of positive electrode materials after discharge of the cell to 1.8 V at different current densities of 75 and 300 mA g^{-1} are recorded and presented in supplementary Fig. S12. With increase of discharge current density, the intensity of all peaks in the XRD pattern is decreased which is probably related to the formation of “quasi-crystalline” phase of sodium oxide at higher current density. Similar behavior is also reported in the case of Li-air cells.³³

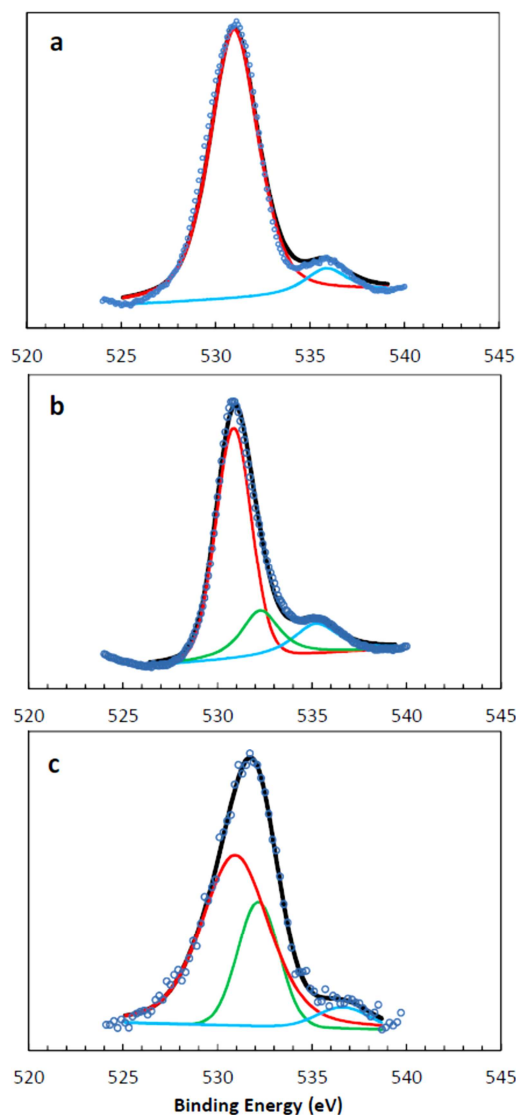


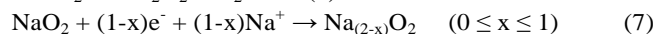
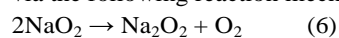
Figure 8: Oxygen 1s spectra of reference sodium peroxide (a); and discharged products resulted at current densities of 75 (b) and 300 mA g^{-1} (c).

Based on discharge curves recorded at different current densities as well as XPS results, it can be concluded that there is a competing reaction between the formation of NaO_2 and

Na_2O_2 , proceeding via equations (1) and (2). The formation of more thermodynamically stable peroxide ion (O_2^{2-}) at lower current densities is favorable, while the formation rate of superoxide ion (O_2^-) is favored at higher current densities. In other words, equation (1) is the dominant discharge reaction at higher current densities while equation (2) is responsible for discharge reaction at lower current densities.

To determine the effect of discharge current density on charge behaviour of Na-air batteries, cells previously discharged to specific capacity of 1.0 Ah g^{-1} at different current densities of 75 to 300 mA g^{-1} , were charged back at constant current density of 40 mA g^{-1} . The resultant curves are shown in Fig. 7b. As the discharge current density increases from 75 to 300 mA g^{-1} , the charge capacity related to the first charge step (the decomposition of NaO_2) increases. The increase in the first charge step coupled with the observed increase in current density indicates that the formation of NaO_2 is favored at higher current densities. Recently, a computational study on the charging mechanism of Li-air cells demonstrated that the formation of off-stoichiometric phase of $\text{Li}_{2-x}\text{O}_2$ is kinetically favorable in order to reduce the charging overpotential of the cell,³² which has also been confirmed experimentally.³³⁻³⁵ Similarly, the formation of deficient phase sodium peroxide with the general formula of $\text{Na}_{2-x}\text{O}_2$ ($0 < x < 1$) at higher discharge current densities is highly probable, especially since the oxygen-rich phase of sodium oxide (NaO_2) is more stable than lithium's counterpart.

To better understand the charge behavior, Na-air cells were subjected to discharge under different limited capacities, from 250 to 1000 mAh g^{-1} , at an elevated current density of 300 mA g^{-1} and then charged back at a constant current density of 75 mA g^{-1} . The resultant charge-discharge curves are depicted in Fig. 9a. A plateau can be observed under lower potentials while two ill-defined plateaus are observed at middle and higher potentials during the charge process of the cell discharged to 250 mAh g^{-1} . However, an increase in the discharge capacity limit from 500 to 1000 mAh g^{-1} , results in a more pronounced plateau at middle and higher potentials. With an increase in discharge capacity limit the charge capacity corresponding to the lower potential plateau subsequently increases. However, an increase of discharge capacity limit also results in an increase to charge capacity corresponding to the middle and higher potential plateaus as well. The appearance of the middle and higher discharge plateaus with increasing discharge capacity limit indicates that chemical composition of the discharge products is changing. Since the formation of NaO_2 is favorable at higher current densities, and that the thermodynamic stability of Na_2O_2 is higher (vide supra), it can be concluded that disproportionation reaction of NaO_2 is responsible for the change in chemical composition seen for the discharge products as well as the appearance of different plateaus during the charge process. Such disproportionation reactions can be performed either chemically or electrochemically at the positive electrode via the following reaction mechanism:



The discharge/charge curves restricted to the low discharge capacity (250 mAh g^{-1}) can also be compared with cyclic voltammetry (CV) curve (supplementary Fig. S13). The CV curve show a sloping region in cathodic and two distinct peaks around 2.8 and 3.6 V in anodic cycle related to the oxygen reduction and evolution reactions which are in accordance with discharge/charge curves, respectively. Based on the results obtained from charge-discharge curves at various current densities and different discharge capacity limits, multiple charge steps can be attributed to the decomposition reaction of different phases of sodium oxides. The lower potential charge plateau is related to a decomposition reaction of oxygen-rich phased sodium superoxide ($x \approx 1$); the middle potential charge plateau is related to decomposition of deficient phase sodium peroxide ($0 < x < 1$); while the higher potential charge plateau is related to decomposition of sodium-rich phased sodium peroxide ($x \approx 0$). In addition, the first three limited discharge and charge curves of Na-air cell recorded at a current density of 150 mA g^{-1} is depicted in Fig. 9b. All consecutive cycles show complete charging with similar profiles. However, the discharge capacity starts to drop down at higher cycle numbers, mainly due to the mechanically failure of the positive electrode material as a result of binder decomposition.

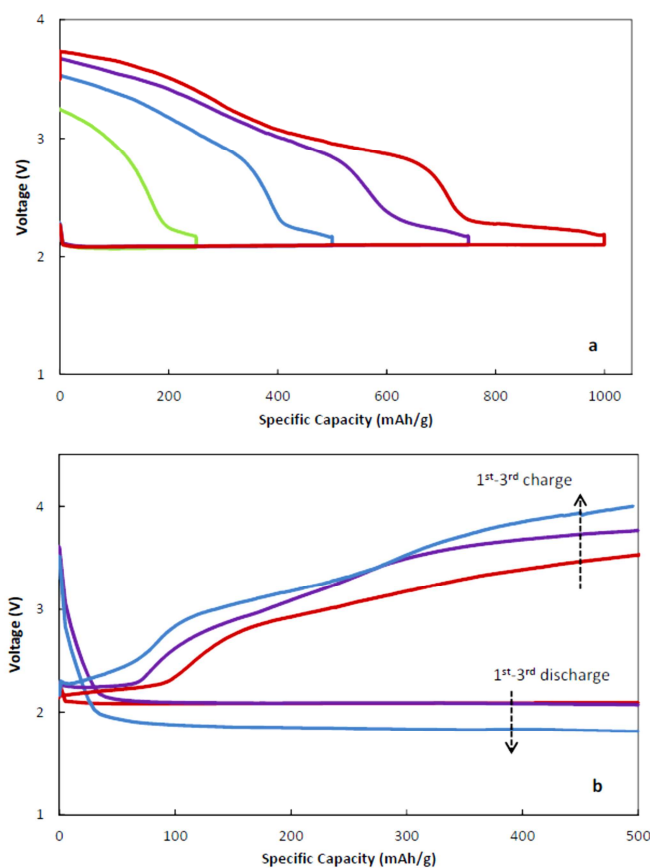


Figure 9: Limited discharge (from 250 to 1000 mAh g^{-1}) and charge curves of Na-air cells using NH_3 -treated carbon material with 85% mass loss as cathode electrode recorded at constant discharge and charge current densities of 300 and 75 mA g^{-1} , respectively (a); First three limited discharge and charge curves of Na-air cell recorded at current density of 150 mA g^{-1} (b).

The present study demonstrates the effects of discharge reaction kinetics on the chemical composition as well as charge characteristics of Na-air battery system. The results suggest that the charge overpotential and efficiency of the cell can be controlled by modifying kinetic parameters related to the discharge reaction. The discharge process of Na-air cells at elevated current densities results in an increase to the amount of NaO₂ produced during discharge as well as decreases the charge reaction overpotential. However it also increases the chemical disproportionation reaction of NaO₂.

Similar results are also reported in Li-air battery system. Nazar et al.³⁵ observed lower charge overpotentials for the Li-air cells discharged at higher current densities. Formation of a defective lithium peroxide phase has been mentioned to be responsible for lowered charge overpotential. Further evidences toward the formation of a superoxide-like species were also reported by Zhai et al.³⁶ and Yang et al.³⁷, indicating the existence of similar chemistry occurring between the Li- and Na-air battery systems. On the other side, more thermodynamic stability of sodium superoxide phase leads to less activity of the discharge product of Na-air cell toward the carbon substrate and hence results in lesser amounts of parasitic side products and lower charge overpotential in Na-air cell which has been called as “cleaner” chemistry by McCloskey et al.¹⁷

It should be also emphasized that the experimental conditions have a great influence on the chemistry of Na- and Li-air cells via altering the kinetic factors involving in the discharge and charge reactions of the cells. More kinetic studies are required to further understand the chemistry behind these cells and the major affecting parameters to control the chemical composition and charge overpotential of the cells.

Conclusion

In summary, discharge capacity, morphological changes and chemical composition of discharge products produced by a Na-air battery system has been investigated in detail and the study was based around the use of a specifically-design and heat-treated carbon material as oxygen diffusion electrode. The specific discharge capacity of the electrode materials with varying specific surface areas demonstrated that discharge capacity is strongly dependent on electrode surface area. In addition, the result revealed that the morphology of the discharge product is also strongly dependent on surface area as well as pore size. The edge planes of carbon substrate were proposed to serve as nucleation sites for the formation of a solid-state discharge product in the Na-air battery system. XRD, Raman, FTIR and XPS analysis of Na-air batteries indicated that both sodium peroxide and superoxide are produced during discharge cycles of the cell and decomposed at different charge steps. In addition, the formation of a deficient phased sodium peroxide (Na_{2-x}O₂, 0 < x < 1) is showed to be likely. Cells discharged at different current densities also exhibited different charge profiles accompanied by a different chemical composition for the discharge product.

3. Experimental

3.1 Positive electrode material preparation

The positive electrode materials were prepared using commercial carbon black (N330). The carbon black was heat-treated under NH₃ or CO₂ (with or without H₂) atmospheres at elevated temperatures. The preparation procedure is fully described elsewhere.¹⁹ Briefly, precise amount of carbon black were heat-treated in a fused silica reactor under NH₃ or CO₂ atmosphere at 1050°C under varying durations. A small portion of the CO₂-treated samples was further pyrolysed under H₂ at 950°C to remove oxygen containing functional groups introduced by CO₂-treatment. Heat-treatment of carbon black removes disordered graphitic structures from the carbon, producing a porous carbon structure. The amount of the carbon mass lost during the heat-treatment was measured using initial and final masses and are presented in supplementary Table S1. The SEM micrographs of N330 and heat-treated carbons (under NH₃ atmosphere) are also shown in supplementary Fig. S14.

3.2 Physical characterizations

Morphological studies were performed by Hitachi S-4800 field-emission scanning electron microscope (SEM) operated at 10.0 kV. N₂ adsorption/desorption isotherms were obtained using a Folio Micromeritics TriStar II Surface Area and Pore Size Analyzer. Fourier transform infra-red (FTIR) spectra and Raman scattering spectra were recorded using a Nicolet 380 and a HORIBA Scientific LabRAM HR Raman spectrometer system equipped with a 532.4 nm laser, respectively. For the FTIR measurements, the sealed testing box containing Na-air cells were moved to an argon-filled glove box (MBRUAN, with water and oxygen contents below 0.1 ppm) and the KBr disks containing 1%w/w of electrode materials were prepared in glove box. Then, the prepared KBr disks were sealed and moved to the FTIR measurement chamber, while nitrogen gas was flushing into the chamber. For Raman analysis, the tested Na-air cells were moved to the glove box and the positive electrode materials were squeezed and sealed between two pieces of glass slide. The Raman analysis was performed on 5 spots of the sealed samples. X-Ray diffractograms were obtained using a Bruker D8 Advance (Cu-K α source, 40 kV, 40 mA). For the XRD measurements, The Na-air cells were moved to the glove box after testing, and the positive electrode materials of at least 4 cells were collected and placed into an air-sensitive XRD sample holder. XPS measurements were made using a glove box-equipped Omicron XM1000 X-ray tube with Al K α source (1486.7 eV) under operating pressure of 10⁻¹⁰ Torr. In the case of XPS measurements, positive electrodes of Na-air cells were washed with the same solvent that used for preparing the electrolyte. Afterward, the electrodes were dried and sealed inside the glove boxed and then moved to the XPS place, where the samples were opened in the second glove box and directly introduced to the XPS chamber. A nickel mesh was used to correct the charging effect. The samples were only kept under pure argon atmosphere for all

analytical measurements, without any exposure to the atmospheric air.

3.3 Electrochemical Measurements

Gas diffusion electrodes were prepared by casting a mixture of carbon materials and Polyvinylidene fluoride (PVDF, Alfa Aesar) with a weight ratio of 9:1 on a separator (Celgard 3500). The electrodes were 3/8 inch in diameter with a loading of ~0.25 mg. Swagelok type cells comprised of sodium foil anode, Celgard 3500 separator, different cathodes and a stainless steel mesh as current collector were used to carry out electrochemical measurements. A fresh sodium foil was prepared with the aid of a homemade press machine using the sodium metal stick (from Aldrich) as starting sodium metal inside the argon-filled glove box. The electrolyte used in this study was a 0.5 M sodium triflate (NaSO₃CF₃ 98%, Aldrich) dissolved in diethylene glycol diethyl ether (reagent grade ≥98%, Aldrich). Sodium triflate electrolyte salt was dried at 80 °C under vacuum for 48 hours and the water content of diethylene glycol diethyl ether solvent was removed using molecular sieves for at least 10 days. The assembled Na-air cells were placed into a homemade testing box inside the glove box and then transferred to the testing room. The argon content of testing box was moderately vacuumed out and then pure oxygen (purity 4.3) purged into the box. The pressure of testing box was kept at 1.0 atm during the electrochemical tests. Discharge/charge characteristics were performed using an Arbin BT-2000 battery station at room temperature (25 °C).

Acknowledgment

This research was supported by Natural Sciences and Engineering Research Council of Canada, Canada Research Chair Program, Canada Foundation for Innovation and the University of Western Ontario. The authors are also indebted to Andrew Lushington for the discussion.

Notes and references

^a Department of Mechanical and Materials Engineering, University of Western Ontario, London, Ontario N6A 5B9, Canada.

^b Department of Chemistry, University of Western Ontario, London, Ontario N6A 5B7, Canada.

^c Canadian Light Source, Saskatoon S7N 0X4, Canada.

*Corresponding author: Xueliang Sun; E-mail: xsun@eng.uwo.ca

Electronic Supplementary Information (ESI) available: Extended characterization results, including electrochemical data, SEM micrographs, XRD and XPS data. See DOI: 10.1039/b000000x/

- Girishkumar, G.; McCloskey, B.; Luntz, A. C.; Swanson, S.; Wilcke, W. *J. Phys. Chem. Lett.* 2010, **1**, 2193-2203.
- Goodenough, J. B.; Kim, Y. *Chem. Mater.* 2010, **22**, 587-603.
- Wagner, F. T.; Lakshmanan, B.; Mathias, M. F. *J. Phys. Chem. Lett.* 2010, **1**, 2204-2219.

- Ogasawara, T.; Debart, A.; Holzapfel, M.; Novak, P.; Bruce, P. G. *J. Am. Chem. Soc.* 2006, **128**, 1390-1393.
- Lu, Y. C.; Gallant, B. M.; Kwabi, D. G.; Harding, J. R.; Mitchell, R. R.; Whittingham, M. S.; Shao-Horn Y. *Energy Environ. Sci.* 2013, **6**, 750-768.
- Kraytsberg, A.; Ein-Eli, Y. *J. Power Sources* 2011, **196**, 886-893.
- Wang, J.; Li, Y.; Sun, X. *Nano Energy* 2013, **2**, 443-467.
- Peng, Z.; Freunberger, S. A.; Chen, Y.; Bruce, P. G. *Science* 2012, **337**, 563-566.
- Sun, Q.; Yang, Y.; Fu, Z. W. *Electrochem. Commun.* 2012, **16**, 22-25.
- Liu, W.; Sun, Q.; Yang, Y.; Xie, J. Y.; Fu, Z. W. *Chem. Commun.* 2013, **49**, 1951-1953.
- Kim, J.; Lim, H. D.; Gwon, H.; Kang, K. *Phys. Chem. Chem. Phys.* 2013, **15**, 3623-3629.
- Hartmann, P.; Bender, C. L.; Vracar, M.; Katharina Dürr, A.; Garsuch, A.; Janek, J.; Adelhelm, P. *Nat. Mater.* 2013, **12**, 228-232.
- Hartmann, P.; Bender, C. L.; Sann, J.; Katharina Dürr, A.; Jansen, M.; Janek, J.; Adelhelm, P. *Phys. Chem. Chem. Phys.* 2013, **15**, 11661-11672.
- Hartmann, P.; Grübl, D.; Sommer, H.; Janek, J.; Bessler, W. G.; Adelhelm, P. *J. Phys. Chem. C* 2014, **118**, 1461-1471.
- Bender, C. L.; Hartmann, P.; Vracar, M.; Adelhelm, P.; Janek, J. *Adv. Energy Mater.* DOI: 10.1002/aenm.201301863.
- Jian, Z.; Chen, Y.; Li, F.; Zhang, T.; Liu, C.; Zhou, H. *J. Power Sources* 2014, **251**, 466-469.
- McCloskey, B. D.; Garcia, J. M.; Luntz, A. C. *J. Phys. Chem. Lett.* 2014, **5**, 1230-1235.
- Kang, S.; Mo, Y.; Ong, S. P.; Ceder, G. *Nano Lett.* 2014, **14**, 1016-1020.
- Li, Y.; Li, X.; Geng, D.; Tang, Y.; Li, R.; Dodelet, J. P.; Lefevre, M.; Sun, X. *Carbon* 2013, **64**, 170-177.
- Li, X.; Li, X.; Banis, M.; Wang, B.; Lushington, A.; Cui, X.; Li, R.; Sham, T. K.; Sun, X. *J. Mater. Chem. A* 2014, DOI: 10.1039/C4TA02007C.
- Lefèvre, M.; Proietti, E.; Jaouen, F.; Dodelet, J. P. *Science* 2009, **3**, 71-74.
- Jaouen, F.; Dodelet, J. P. *J. Phys. Chem. C* 2007, **111**, 5963-5970.
- Mitchell, R. R.; Gallant, B. M.; Shao-Horn, Y.; Thompson, C. V. *J. Phys. Chem. Lett.* 2013, **4**, 1060-1064.
- Gallant, B. M.; Kwabi, D. G.; Mitchell, R. R.; Zhou, J.; Thompson, C. V.; Shao-Horn, Y. *Energy Environ. Sci.* 2013, **6**, 2518-2528.
- Black, R.; Hyoung Oh, S.; Lee, J. H.; Yim, T.; Adams, B.; Nazar, L. F. *J. Am. Chem. Soc.* 2012, **134**, 2902-2905.
- Wen, R.; Hong, M.; Byon, H. R. *J. Am. Chem. Soc.* 2013, **135**, 10870-10876.
- Banks, C. E.; Compton, R. G. *Analyst* 2006, **131**, 15-21.
- Evans, J. C. *J. Chem. Soc. D*, 1969, 682-683.
- Brame Jr., E. G.; Cohen, S.; Margrave, J. L.; Meloche, V. W. *J. Inorg. Nucl. Chem.* 1957, **4**, 90-92.
- Peled, E.; Golodnitsky, D.; Hadara, R.; Mazora, H.; Goora, M.; Burstein L. *J. Power Sources* 2013, **244**, 771-776.
- Shek, M. L.; Hrbek, J.; Sham, T. K.; Xu, G. Q. *J. Vac. Sci. Technol. A* 1991, **9**, 1640-1644.
- Kang, S.; Mo, Y.; Ong, S. P.; Ceder, G. *Chem. Mater.* 2013, **25**, 3328-3336.

- 33 Jung, H. G.; Hassoun, J.; Park, J. B.; Sun, Y. K.; Scrosati, B. *Nat. Chem.* 2012, **4**, 579-585.
- 34 Jung, H. G.; Kim, H. S.; Park, J. B.; Oh, I. H.; Hassoun, J.; Yoon, C. S.; Scrosati, B.; Sun, Y. K. *Nano Lett.* 2012, **12**, 4333-4335.
- 35 Adams, B. D.; Radtke, C.; Black, R.; Trudeau, M. L.; Zaghbi, K.; Nazar, L. F. *Energy Environ. Sci.* 2013, **6**, 1772-1778.
- 36 Zhai, D.; Wang, H. H.; Yang, J.; Lau, K. C.; Li, K.; Amine, K.; Curtiss, L. A. *J. Am. Chem. Soc.* 2013, **135**, 15364-15372.
- 37 Yang, J.; Zhai, D.; Wang, H. H.; Lau, K. C.; Schlueter, J. A.; Du, P.; Myers, D. J.; Sun, Y. K.; Curtiss, L. A.; Amine, K. *Phys. Chem. Chem. Phys.* 2013, **15**, 3764-3771.